

# An evidence of mass dependent differential kinetic freeze-out scenario observed in Pb-Pb collisions at 2.76 TeV

Hai-Ling Lao<sup>a</sup>, Hua-Rong Wei<sup>a</sup>, Fu-Hu Liu<sup>a,1</sup>, and Roy A. Lacey<sup>b,2</sup>

<sup>a</sup>*Institute of Theoretical Physics, Shanxi University, Taiyuan, Shanxi 030006, China*

<sup>b</sup>*Departments of Chemistry & Physics, Stony Brook University, Stony Brook, NY 11794, USA*

**Abstract:** Transverse momentum spectra of different particles produced in mid-rapidity interval in lead-lead (Pb-Pb) collisions with different centrality intervals, measured by the ALICE Collaboration at center-of-mass energy per nucleon pair  $\sqrt{s_{NN}} = 2.76$  TeV, are conformably and approximately described by the Tsallis distribution. The dependences of parameters (effective temperature, entropy index, and normalization factor) on event centrality and particle rest mass are obtained. The source temperature at the kinetic freeze-out is obtained to be the intercept in the linear relation between effective temperature and particle rest mass, while the particle (transverse) flow velocity in the source rest frame is extracted to be the slope in the linear relation between mean (transverse) momentum and mean moving mass. It is shown that the source temperature increases with increase of particle rest mass, which exhibits an evidence of mass dependent differential kinetic freeze-out scenario or multiple kinetic freeze-out scenario.

**Keywords:** Source temperature, kinetic freeze-out scenario, mass dependent differential kinetic freeze-out scenario

**PACS:** 12.38.Mh, 25.75.Dw, 24.10.Pa

## 1 Introduction

High energy nucleus-nucleus (heavy ion) collisions at the large hadron collider (LHC) [1–5] have been providing another excellent environment and condition of high temperature and density, where the new state of matter, namely the quark-gluon plasma (QGP) [6–8], is expected to form and to live for a longer lifetime than that at the relativistic heavy ion collider (RHIC) [9]. Although the RHIC is scheduled to run at lower energies which are around the critical energy of phase transition from hadronic matter to QGP, the LHC is expected to run at higher energies. Presently, the LHC has provided three different types of collisions: proton-proton ( $pp$ ), proton-lead ( $p$ -Pb), and lead-lead (Pb-Pb) collisions at different collision energies. The former two are not expected to form the QGP due to small system, though the deconfinement of quarks and gluons may appear. The latter one is expected to form the QGP due to large system and high energy.

---

<sup>1</sup>E-mail: fuhuliu@163.com; fuhuliu@sxu.edu.cn

<sup>2</sup>E-mail: Roy.Lacey@Stonybrook.edu

It is believed that the QGP is formed in Pb-Pb collisions at the LHC and in nucleus-nucleus collisions at lower energy till dozens of GeV at the RHIC [10, 11]. If mesons are produced in the participant region where violent collision had happened and the QGP is formed, nuclear fragments such as helium or heavier nuclei are expected to emit in spectator region where non-violent evaporation and fragmentation had happened [12–14]. The ALICE Collaboration [15–18] measured together positive pions  $\pi^+$ , positive kaons  $K^+$ , protons  $p$ , deuterons  $d$ , and one of helium isotopes  $^3\text{He}$  in Pb-Pb collisions with different centrality intervals at the LHC. It gives us a chance to describe uniformly different particles. In particular, we are interested in the uniform description of transverse momentum spectra of  $\pi^+$ ,  $K^+$ ,  $p$ ,  $d$ , and  $^3\text{He}$ , so that we can extract the kinetic freeze-out (KFO) temperature of interacting system (i.e. source temperature at KFO).

From source temperature at KFO, we can draw a KFO scenario. There are three different KFO scenarios discussed in literature [3, 19–22]. The single KFO scenario [19] uses one set of parameters for both the spectra of strange and non-strange particles. The double KFO scenario [3, 20] uses a set of parameters for the spectra of strange particles, and another set of parameters for the spectra of non-strange particles. The multi-KFO scenario [21, 22] uses different sets of parameters for different particles with different masses. Naturally, the mass dependent differential KFO scenario [22] belongs to the multi-KFO scenario. It is an open question which KFO scenario describes correctly. We are interested in the study of KFO scenario in the present work. As can be seen from the following sections, our analysis provides an evidence of mass dependent differential KFO scenario.

To extract source temperature at the KFO, we have to describe transverse momentum spectra. More than ten functions are used in the descriptions of transverse momentum spectra. In the present work, we select the Tsallis distribution [23–25] that covers the sum of two or three standard distributions [26, 27] and describes temperature fluctuations among different local equilibrium states. Based on the descriptions of the experimental data of the ALICE Collaboration [15, 16] on Pb-Pb collisions at center-of-mass energy per nucleon pair  $\sqrt{s_{NN}} = 2.76$  TeV, the source temperature at the KFO is obtained to be the intercept in the linear relation between effective temperature and particle rest mass, while the particle (transverse) flow velocity in the source rest frame is extracted to be the slope in the linear relation between mean (transverse) momentum and mean moving mass. If we use other functions, the method is in fact the same. Because of no difference between positive and negative spectra being reported [16], we are just fitting the available positive data in the analysis.

The structure of the present work is as followings. The model and method are shortly described in section 2. Results and discussion are given in section 3. In section 4, we summarize our main observations and conclusions.

## 2 The model and method

We discuss the collision process in the framework of the multisource thermal model [28–30]. According to the model, many emission sources are formed in high energy nucleus-nucleus collisions. We can choose different distributions to describe the emission sources

and particle spectra. These distributions include, but are not limited to, the Tsallis distribution [23–25], the standard (Boltzmann, Fermi-Dirac, and Bose-Einstein) distributions [26], the Tsallis + standard distributions [31–36], the Erlang distribution [28], and so forth.

The Tsallis distribution can be described by two or three standard distributions. The Tsallis + standard distributions can be described by two or three Tsallis distributions [27]. It is needless to choose the standard distributions due to multiple sources (temperatures). It is also needless to choose the Tsallis + standard distributions due to not too many sources (temperatures). A middle way is to choose the Tsallis distribution which describes the temperature fluctuation in a few sources to give an average value. These sources with different excitation degrees can be naturally described by the standard distributions with different effective temperatures, which result from the multisource thermal model [28–30].

The Tsallis distribution has more than one function forms [23–25, 31–38]. In the rest frame of a considered source, we choose a simplified form of the joint probability density function of transverse momentum ( $p_T$ ) and rapidity ( $y$ ),

$$f(p_T, y) \propto \frac{d^2 N}{dy dp_T} = \frac{gV}{(2\pi)^2} p_T \sqrt{p_T^2 + m_0^2} \cosh y \left[ 1 + \frac{q-1}{T} \left( \sqrt{p_T^2 + m_0^2} \cosh y - \mu \right) \right]^{-q/(q-1)}, \quad (1)$$

where  $N$  is the particle number,  $g$  is the degeneracy factor,  $V$  is the volume of emission sources,  $T$  is the temperature which describes averagely a few sources (local equilibrium states),  $q$  is the entropy index which describes the degree of non-equilibrium among different states,  $\mu$  is the chemical potential which is related to  $\sqrt{s_{NN}}$  [39] and can be regarded as 0 at the LHC,  $m_0$  is the rest mass of the considered particle. Generally, the 4-parameter ( $T$ ,  $q$ ,  $\mu$ , and  $V$ ) form of Eq. (1) is capable of reproducing the particle spectra, where  $T$ ,  $q$ , and  $\mu$  are fitted independently for the considered particle species, and  $V$  is related to other parameters.

Eq. (1) results in the transverse momentum probability density function which is an alternative representation of the Tsallis distribution as follows

$$f_{p_T}(p_T) = \frac{1}{N} \frac{dN}{dp_T} = \int_{y_{\min}}^{y_{\max}} f(p_T, y) dy, \quad (2)$$

where  $y_{\max}$  and  $y_{\min}$  denote the maximum and minimum rapidities, respectively. Similarly, Eq. (1) results in the rapidity probability density function in the source rest frame as follows

$$f_y(y) = \frac{1}{N} \frac{dN}{dy} = \int_0^{p_{T\max}} f(p_T, y) dp_T, \quad (3)$$

where  $p_{T\max}$  denotes the maximum transverse momentum.

Under the assumption of isotropic emission in the source rest frame, we have the polar angle probability density function to be

$$f_\theta(\theta) = \frac{1}{2} \sin \theta. \quad (4)$$

Let  $r_1$  and  $r_2$  denote the random numbers distributed uniformly in  $[0,1]$  respectively. We can use the Monte Carlo method to obtain a series of  $p_T$  which satisfies

$$\int_0^{p_T} f_{p_T}(p_T) dp_T < r_1 < \int_0^{p_T + dp_T} f_{p_T}(p_T) dp_T. \quad (5)$$

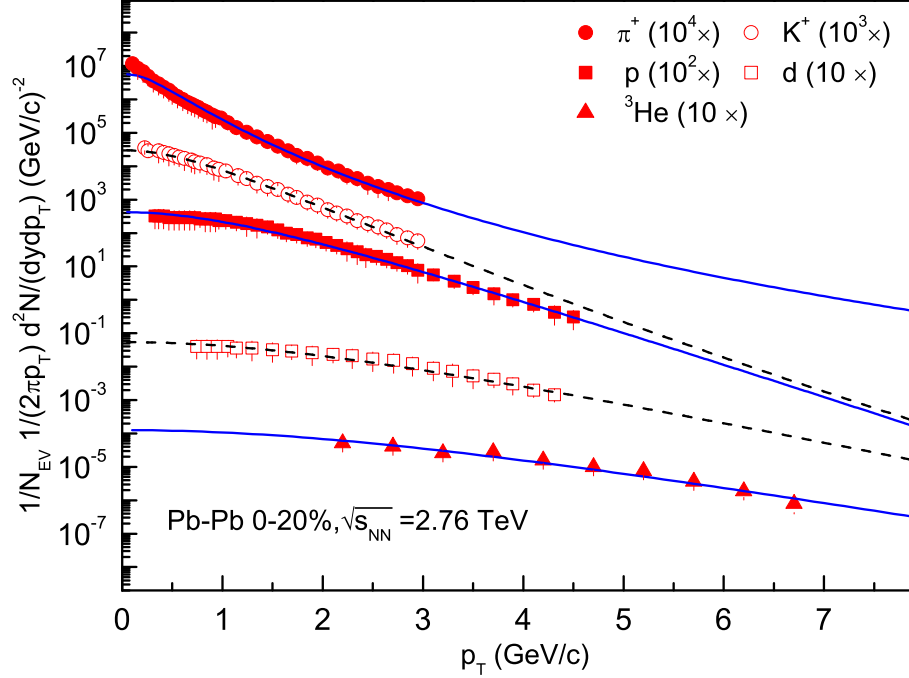


Figure 1. Transverse momentum spectra of  $\pi^+$ ,  $K^+$ ,  $p$ ,  $d$ , and  ${}^3\text{He}$  produced in mid-rapidity interval ( $|y| < 0.5$ ) in Pb-Pb collisions at  $\sqrt{s_{NN}} = 2.76$  TeV. The symbols represent the experimental data of the ALICE Collaboration [16] in centrality interval 0–20%, which are scaled by different amounts marked in the panel. The curves are our results fitted by using the Tsallis distribution based on Eq. (1). In the fitting, the method of least squares is used to obtain the values of related parameters.

The Monte Carlo method results in

$$\theta = 2 \arcsin \sqrt{r_2} \quad (6)$$

due to Eq. (4). Thus, we can obtain a series of values of momentum and energy due to the momentum  $p = p_T / \sin \theta$  and the energy  $E = \sqrt{p^2 + m_0^2}$ . The energy  $E$  is in fact equal to the moving mass  $m$  in the natural unit system. Then, we have the mean moving mass  $\overline{m}$  to be the mean energy  $\overline{E}$ .

### 3 Results and discussion

Figure 1 presents the transverse momentum spectra,  $(1/N_{EV})d^2N/(2\pi p_T dy dp_T)$ , of  $\pi^+$ ,  $K^+$ ,  $p$ ,  $d$ , and  ${}^3\text{He}$  produced in mid-rapidity interval ( $|y| < 0.5$ ) in Pb-Pb collisions at  $\sqrt{s_{NN}} = 2.76$  TeV, where  $N_{EV}$  denotes the number of events. The symbols represent the experimental data of the ALICE Collaboration [16] in centrality interval 0–20%, which are scaled by different amounts marked in the panel. The curves are our results fitted by using the Tsallis distribution based on Eq. (1) at mid-rapidity ( $y = 0$ ). In the fitting, the method of least squares is used. The values of related parameters  $T$ ,  $q$ , and  $N_0$  are listed

in Table 1 with values of  $\chi^2$  per degree of freedom ( $\chi^2/\text{dof}$ ), where

$$N_0 = \frac{gV}{(2\pi)^3} \int_0^{p_{T\max}} \int_{y_{\min}}^{y_{\max}} \sqrt{p_T^2 + m_0^2} \cosh y \left[ 1 + \frac{q-1}{T} (\sqrt{p_T^2 + m_0^2} \cosh y - \mu) \right]^{-q/(q-1)} dy dp_T \quad (7)$$

is the normalization factor which is used to compare the normalized curve with experimental data. One can see that the Tsallis distribution describes conformably and approximately  $\pi^+$ ,  $K^+$ ,  $p$ ,  $d$ , and  $^3\text{He}$  spectra. The effective temperature increases with increase of particle rest mass.

Table 1. Values of  $T$ ,  $q$ ,  $N_0$ , and  $\chi^2/\text{dof}$  corresponding to the curves in Figures 1–3, where the data set for  $^3\text{He}$  in Figure 1 is the same as that for centrality interval 0–20% in Figure 3 [16], which renders the same values of parameters.

| Figure   | Type 1        | Type 2        | $T$ (GeV)         | $q$                 | $N_0$                              | $\chi^2/\text{dof}$ |
|----------|---------------|---------------|-------------------|---------------------|------------------------------------|---------------------|
| Figure 1 | 0–20%         | $\pi^+$       | $0.134 \pm 0.012$ | $1.0980 \pm 0.0100$ | $228.512 \pm 81.588$               | 0.163               |
|          |               | $K^+$         | $0.271 \pm 0.020$ | $1.0210 \pm 0.0060$ | $22.238 \pm 6.254$                 | 0.082               |
|          |               | $p$           | $0.411 \pm 0.033$ | $1.0010 \pm 0.0009$ | $4.709 \pm 1.502$                  | 0.077               |
|          |               | $d$           | $0.645 \pm 0.068$ | $1.0010 \pm 0.0008$ | $0.010 \pm 0.003$                  | 0.117               |
|          |               | $^3\text{He}$ | $0.781 \pm 0.085$ | $1.0013 \pm 0.0009$ | $(2.930 \pm 0.453) \times 10^{-5}$ | 1.162               |
| Figure 2 | $d$           | 0–10%         | $0.659 \pm 0.039$ | $1.0005 \pm 0.0004$ | $(1.184 \pm 0.105) \times 10^{-2}$ | 2.359               |
|          |               | 10–20%        | $0.634 \pm 0.028$ | $1.0004 \pm 0.0003$ | $(9.469 \pm 0.855) \times 10^{-3}$ | 1.689               |
|          |               | 20–40%        | $0.582 \pm 0.031$ | $1.0007 \pm 0.0006$ | $(6.256 \pm 0.742) \times 10^{-3}$ | 0.863               |
|          |               | 40–60%        | $0.485 \pm 0.056$ | $1.0010 \pm 0.0008$ | $(2.937 \pm 0.612) \times 10^{-3}$ | 0.244               |
|          |               | 60–80%        | $0.345 \pm 0.021$ | $1.0010 \pm 0.0008$ | $(9.317 \pm 1.682) \times 10^{-4}$ | 0.214               |
|          |               | $pp$          | $0.273 \pm 0.014$ | $1.0030 \pm 0.0010$ | $(4.143 \pm 0.545) \times 10^{-5}$ | 0.831               |
| Figure 3 | $^3\text{He}$ | 0–20%         | $0.781 \pm 0.085$ | $1.0013 \pm 0.0009$ | $(2.930 \pm 0.453) \times 10^{-5}$ | 1.162               |
|          |               | 20–80%        | $0.670 \pm 0.032$ | $1.0021 \pm 0.0015$ | $(6.100 \pm 0.951) \times 10^{-6}$ | 1.379               |

Figure 2 is similar to Figure 1, but it shows the results for  $d$  in different centrality intervals, which are scaled by different amounts marked in the panels. At the same time, the result in  $pp$  collisions at  $\sqrt{s} = 7$  TeV is presented for comparison, where  $\sqrt{s}$  is a simplified form of  $\sqrt{s_{NN}}$  for  $pp$  collisions. Figure 3 is similar to Figure 1, but it shows the results for  $^3\text{He}$  in centrality intervals 0–20% and 20–80%, where the data set for 0–20% is the same as that for  $^3\text{He}$  in Figure 1 [16]. The related parameter values are listed in Table 1 with values of  $\chi^2/\text{dof}$ . One can see that the Tsallis distribution describes approximately the experimental data of  $d$  produced in Pb-Pb collisions with different centrality intervals at the LHC. The effective temperature extracted from  $d$  spectra decreases with decrease of centrality (or increase of centrality percentage).

To study the change trends of parameters with centrality interval ( $C$ ) of event and rest mass of particle, Figure 4 gives the dependences of (a)  $T$  on  $C$  for  $d$  in events with different centrality intervals and (b)  $T$  on  $m_0$  for particles in events with centrality interval 0–20%, where only the result for  $d$  in Figure 4(a) is available due to the experimental result [16]. The symbols represent the parameter values extracted from Figures 1 and 2 and listed in Table 1, and the curves are our results fitted by the method of least squares. The curve

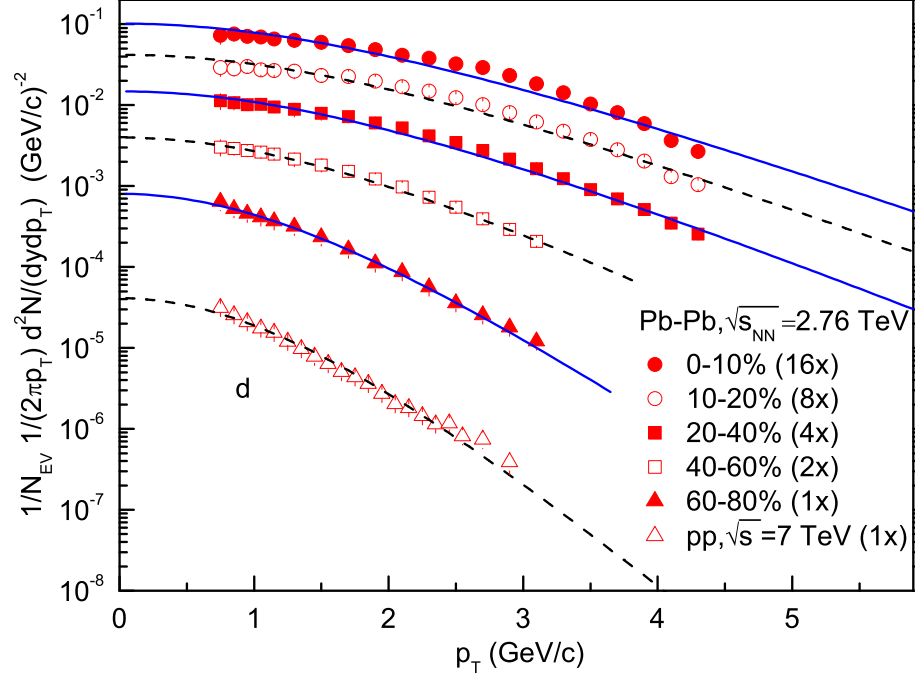


Figure 2. The same as for Figure 1, but showing the results of  $d$  in Pb-Pb collisions with different centrality intervals and in  $pp$  collisions.

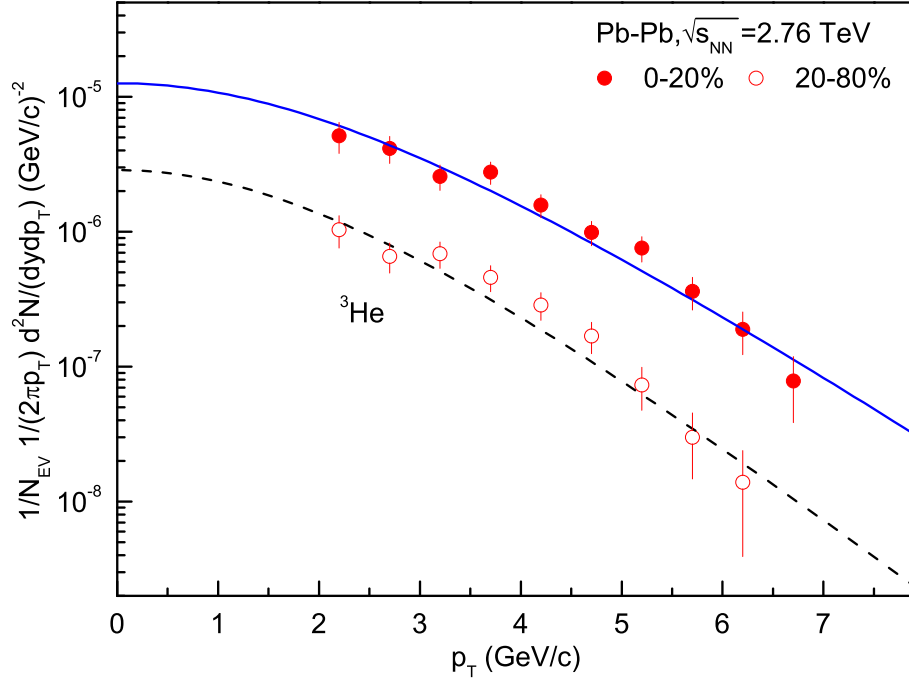


Figure 3. The same as for Figure 1, but showing the results of  $^3\text{He}$  in Pb-Pb collisions with two centrality intervals.

in Figure 4(a) is described by

$$T = -(0.000059 \pm 0.000005)C^2 - (0.0012 \pm 0.0002)C + (0.668 \pm 0.005) \quad (8)$$

with  $\chi^2/\text{dof}=0.927$ , where  $T$  is in the units of GeV. The solid, dotted, and dashed curves in Figure 4(b) are linear fittings for i)  $\pi^+$ ,  $K^+$ , and  $p$ ; ii)  $\pi^+$ ,  $K^+$ ,  $p$ , and  $d$ ; and iii)  $\pi^+$ ,  $K^+$ ,  $p$ ,  $d$ , and  ${}^3\text{He}$ , which are described by

$$T = (0.091 \pm 0.009) + (0.345 \pm 0.014)m_0, \quad (9)$$

$$T = (0.115 \pm 0.017) + (0.291 \pm 0.016)m_0, \quad (10)$$

and

$$T = (0.148 \pm 0.032) + (0.241 \pm 0.020)m_0, \quad (11)$$

with  $\chi^2/\text{dof}=0.429$ , 2.091, and 5.869, respectively, where  $m_0$  is in the units of  $\text{GeV}/c^2$ .

The intercept in Eq. (9) is regarded as the KFO temperatures [40–43] of emission source, which is 0.091 GeV corresponding to massless particles, when the source produces  $\pi^+$ ,  $K^+$ , and  $p$ . Including  $d$  causes a large intercept (0.115 GeV) in Eq. (10), while including  $d$  and  ${}^3\text{He}$  causes a larger intercept (0.148 GeV) in Eq. (11). Although the errors in intercepts are large, these results render that the KFO temperature increases with increase of particle rest mass. This is an evidence of mass dependent differential KFO scenario or multiple KFO scenario [21, 22].

The blast-wave model [44] gives the KFO temperature extracted from  $d$  spectra being 0.077–0.124 GeV and from  ${}^3\text{He}$  spectra being 0.101 GeV [16] which are comparable with the present work. In particular, the blast-wave model gives the KFO temperature in central collisions being less than that in peripheral collisions [16], which is inconsistent with Figure 4(a) which shows an opposite result on correlation between effective temperature and centrality. Although the result of blast-wave model can be explained as that the interacting system in central collisions undergoes a longer kinetic evolution which results in a lower KFO temperature comparing with peripheral collisions, the present result can be explained as that the interacting system in central collisions stays in a higher excitation state comparing with peripheral collisions.

On the other hand, we have used an alternative method to extract indirectly the KFO temperature based on the linear relation between effective temperature and rest mass [40–43]. The evidence coming from similar analyses in RHIC and LHC experiments [45, 46], where the fit parameters have been studied also against centrality, even down to data of  $d$ -nucleus or  $pp$  collisions, confirms that the KFO temperature in central collisions is less than that in peripheral collisions, which is inconsistent with the present work. For central and peripheral collisions, the relative size of KFO temperature obtained in the present work is similar to those of the chemical freeze-out temperature and effective temperature. We would like to point out that the present work is qualitatively consistent with ref. [19], where the Tsallis + blast-wave model is used at RHIC energy.

Although the interpretation of the Tsallis distribution is still controversial, at least in the field of concern here, it could be interesting to learn the behavior of non-additive entropy. In Figure 5, the dependences of (a)  $q$  on  $C$  for  $d$  in events with different centrality intervals and (b)  $q$  on  $m_0$  for different particles in events with centrality interval 0–20%

are given, where only the result for  $d$  in Figure 5(a) is available due to the experimental result [16]. The symbols represent the parameter values extracted from Figures 1 and 2 and listed in Table 1. For  $d$  in events with different centrality intervals, the values of  $q$  are foregone to be consistent with one [Figure 5(a)]. For the events with centrality interval 0–20%,  $\pi^+$  corresponds to a larger  $q$  than others [Figure 5(b)]. This renders that the production of pions is more polygenetic than others. Because of the most values of  $q$  being small, the interacting system stays approximately in an equilibrium state.

In fact, the ranges of most  $p_T$  spectra considered in Pb-Pb collisions in the present work are narrow, which result mainly from the soft process which is a single source and can be described by the standard distribution. If we study wide  $p_T$  spectra, both the soft and hard processes have to be considered. We need two or three standard distributions, the standard distribution + a power law, or the Tsallis distribution with large  $q$  to describe the wide spectra. The situation for  $pp$  collisions is similar to Pb-Pb collisions. The advantage of Tsallis distribution will appear in description of the wide spectra. For the narrow spectra, both the standard distribution and the Tsallis distribution with small  $q$  are satisfied. However, we use the Tsallis distribution due to its potential application in wide  $p_T$  spectra. In addition, the STAR experiment already tried a Tsallis-like study, publishing also a Tsallis + blast-wave model-based interpretation of their data [9]. The ALICE data, on the other hand, have been compared to a blast-wave + thermal-based fit [16]. In both cases the agreement is very good. These facts render that the Tsallis distribution has a wide application in high energy physics.

In Figure 6, the dependences of (a)  $N_0$  on  $C$  for  $d$  in events with different centrality intervals and (b)  $N_0$  on  $m_0$  for different particles in events with centrality interval 0–20% are given, where only the result for  $d$  in Figure 6(a) is available due to the experimental result [16]. The symbols represent the parameter values extracted from Figures 1 and 2 and listed in Table 1. The curves are our results fitted by the method of least squares, which are described by

$$N_0 = (0.0166 \pm 0.0004) \exp[-(0.019 \pm 0.001)C] - (0.0033 \pm 0.0002) \quad (12)$$

and

$$N_0 = (580.207 \pm 62.425) \exp[-(5.912 \pm 0.118)m_0] \quad (13)$$

with  $\chi^2/\text{dof}=0.572$  and  $1.712$  respectively. It is shown that  $N_0$  decreases with decrease of centrality. The larger the particle rest mass is, the lower the production probability is. Although  $N_0$  is only a normalization factor and the data are not cross-section, they are proportional to the volumes of sources producing different particles. Therefore, studying  $N_0$  dependence is significative.

To extract the transverse flow velocity, we display the dependence of mean transverse momentum ( $\langle p_T \rangle$ ) on mean moving mass ( $\overline{m}$ ) in Figure 7(a). The symbols represent the values of  $\langle p_T \rangle$  and  $\overline{m}$  for different particles calculated by using the Monte Carlo method in the source rest frame. The solid, dotted, and dashed curves in Figure 7(a) are linear fittings for i)  $\pi^+$ ,  $K^+$ , and  $p$ ; ii)  $\pi^+$ ,  $K^+$ ,  $p$ , and  $d$ ; and iii)  $\pi^+$ ,  $K^+$ ,  $p$ ,  $d$ , and  ${}^3\text{He}$ , which are described by

$$\langle p_T \rangle = (0.108 \pm 0.006) + (0.502 \pm 0.004)\overline{m}, \quad (14)$$

$$\langle p_T \rangle = (0.124 \pm 0.008) + (0.490 \pm 0.003)\overline{m}, \quad (15)$$



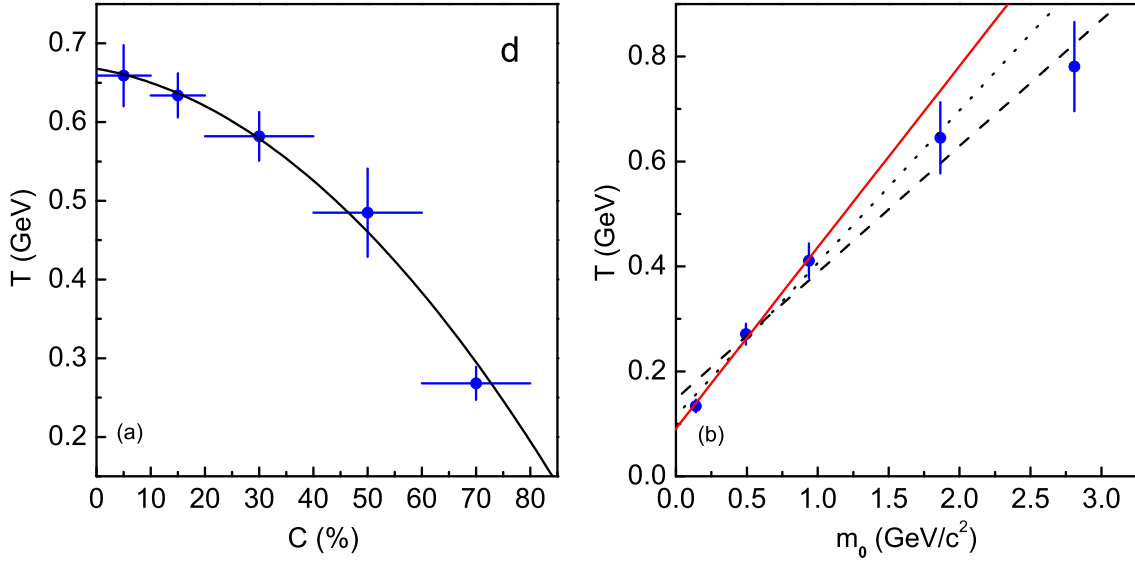


Figure 4. Dependences of (a)  $T$  on  $C$  for  $d$  in events with different centrality intervals and (b)  $T$  on  $m_0$  for particles in events with centrality interval 0–20%. The symbols represent the parameter values listed in Table 1. The curves and lines are our results fitted by the method of least squares.

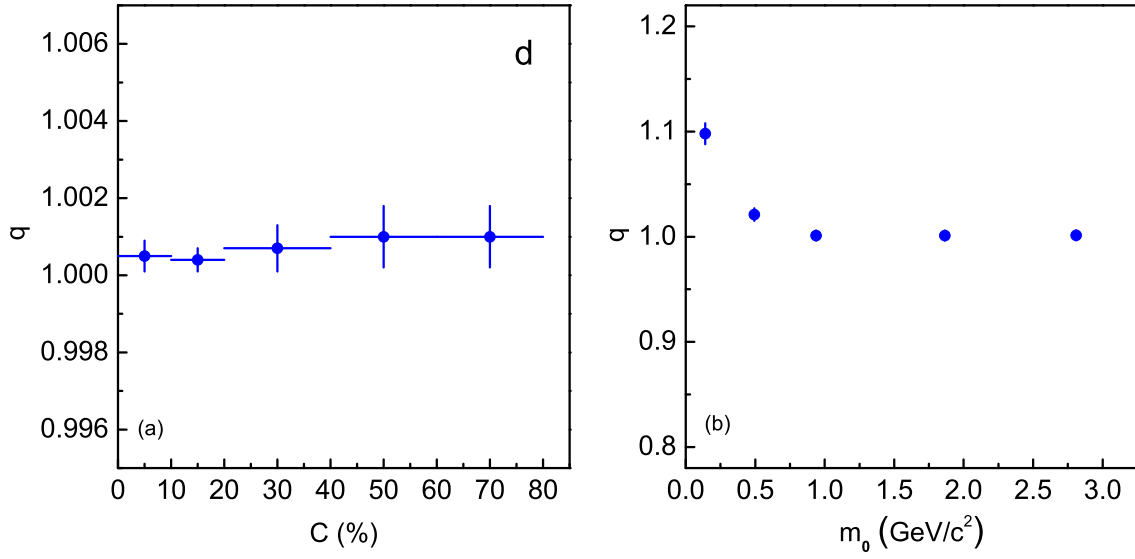


Figure 5. Dependences of (a)  $q$  on  $C$  for  $d$  in events with different centrality intervals and (b)  $q$  on  $m_0$  for particles in events with centrality interval 0–20%. The symbols represent the parameter values listed in Table 1.

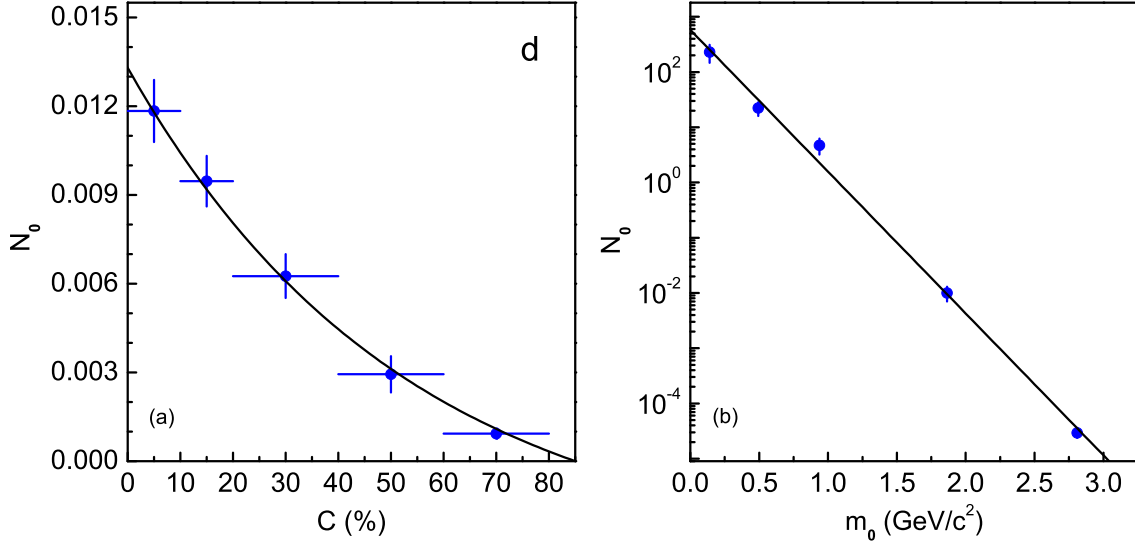


Figure 6. Dependences of (a)  $N_0$  on  $C$  for  $d$  in events with different centrality intervals and (b)  $N_0$  on  $m_0$  for particles in events with centrality interval 0–20%. The symbols represent the parameter values listed in Table 1. The curve and line are our results fitted by the method of least squares.

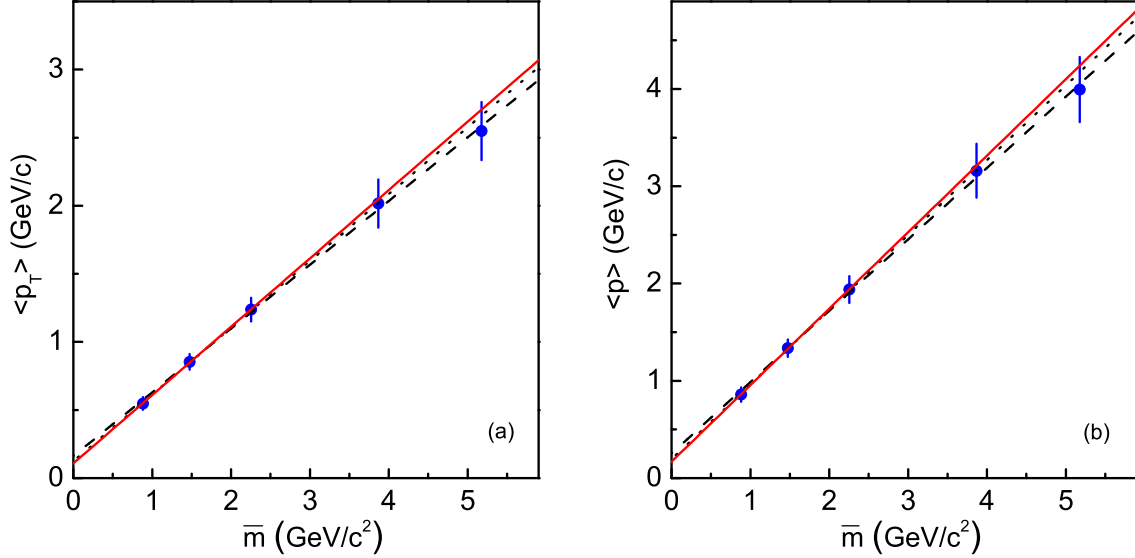


Figure 7. Dependences of (a)  $\langle p_T \rangle$  on  $\bar{m}$  and (b)  $\langle p \rangle$  on  $\bar{m}$  for particles in events with centrality interval 0–20%. The symbols represent the values of  $\langle p_T \rangle$  and  $\langle p \rangle$  at different  $\bar{m}$ , which are calculated by using the Monte Carlo method in the source rest frame. The lines are our results fitted by the method of least squares.

and

$$\langle p_T \rangle = (0.162 \pm 0.029) + (0.468 \pm 0.009)\overline{m}, \quad (16)$$

with  $\chi^2/\text{dof}=0.009$ ,  $0.025$ , and  $0.155$ , respectively, where  $\langle p_T \rangle$  and  $\overline{m}$  are in the units of  $\text{GeV}/c$  and  $\text{GeV}/c^2$  respectively. From the consideration of dimension, the slopes in Eqs. (14)–(16) are regarded as the (average) transverse flow velocity, which is close to  $0.5c$ . Including  $d$  or  $d$  and  ${}^3\text{He}$ , one can see a small decrease in transverse flow velocity. The blast-wave model [44] gives the transverse flow velocity for  $d$  is  $0.38\text{--}0.63c$  and for  ${}^3\text{He}$  is  $0.56\text{--}0.57c$  [16] which is comparable with the present work.

Figure 7(b) is the same as for Figure 7(a), but showing the dependence of mean momentum ( $\langle p \rangle$ ) on  $\overline{m}$ . The values of  $\langle p \rangle$  are calculated by using the Monte Carlo method in the source rest frame, too. The solid, dotted, and dashed curves in Figure 7(b) are linear fittings for i)  $\pi^+$ ,  $K^+$ , and  $p$ ; ii)  $\pi^+$ ,  $K^+$ ,  $p$ , and  $d$ ; and iii)  $\pi^+$ ,  $K^+$ ,  $p$ ,  $d$ , and  ${}^3\text{He}$ , which are described by

$$\langle p \rangle = (0.170 \pm 0.010) + (0.786 \pm 0.006)\overline{m}, \quad (17)$$

$$\langle p \rangle = (0.195 \pm 0.013) + (0.768 \pm 0.005)\overline{m}, \quad (18)$$

and

$$\langle p \rangle = (0.254 \pm 0.046) + (0.733 \pm 0.015)\overline{m}, \quad (19)$$

with  $\chi^2/\text{dof}=0.009$ ,  $0.024$ , and  $0.156$ , respectively, where  $\langle p \rangle$  is in the units of  $\text{GeV}/c$ . From the consideration of dimension, the slopes in Eqs. (17)–(19) are regarded as the (average) flow velocity, which is close to  $(\pi/2)0.5c$  which confirms our very recent work [47]. Including  $d$  or  $d$  and  ${}^3\text{He}$ , one can see a small decrease in flow velocity.

In the above discussions, although KFO temperatures and (transverse) flow velocities are only extracted by us by indirect methods and we have not obtained the straightforward KFO, the present work provides anyhow alternative methods to describe  $p_T$  spectra and to extract indirectly KFO temperature and (transverse) flow velocity. In fact, different functions result in different KFO temperatures. To extract the absolute temperature at KFO, the standard distribution is the best choice. However, we have to use a multi-component standard distribution. Because the mean (transverse) momentum and mean moving mass are independent of models. The (transverse) flow velocity extracted from the slope in the linear relation between mean (transverse) momentum and mean moving mass should be independent of models, too.

In our very recent work [47], the linear relations between  $T$  and  $m_0$ ,  $T$  and  $\overline{m}$ ,  $\langle p_T \rangle$  and  $m_0$ ,  $\langle p_T \rangle$  and  $\overline{m}$ ,  $\langle p \rangle$  and  $m_0$ , as well as  $\langle p \rangle$  and  $\overline{m}$  are studied. It is shown that the intercept in the linear relation between  $T$  and  $m_0$  can be regarded as the KFO temperature, the slope in the linear relation between  $\langle p_T \rangle$  and  $\overline{m}$  can be regarded as the transverse flow velocity, and the slope in the linear relation between  $\langle p \rangle$  and  $\overline{m}$  can be regarded as the flow velocity. In the present work, we use the same treatment to obtain the KFO temperature, transverse flow velocity, and flow velocity in the source rest frame. The present work shows that light particles correspond to low KFO temperature, which reflects that light particles freeze later than heavy particles. At the same time, due to small mass, light particles have larger (transverse) flow velocity than heavy particles.

## 4 Conclusions

We summarize here our main observations and conclusions.

a) The transverse momentum distributions of  $\pi^+$ ,  $K^+$ ,  $p$ ,  $d$ , and  $^3\text{He}$  produced in Pb-Pb collisions at 2.76 TeV with different centrality intervals are conformably analyzed by using the Tsallis distribution. The results calculated by us can fit approximately the experimental data of the ALICE Collaboration. The values of parameters such as the effective temperature, entropy index, and normalization factor are obtained. Small sizes of entropy index show that the interacting system considered in the present work stays approximately in an equilibrium state. The effective temperature extracted from transverse momentum spectra increases with increase of particle rest mass, and decreases with decrease of centrality.

b) We have used an alternative method to extract the kinetic freeze-out temperature of the interacting system based on the linear relation between the effective temperature and particle rest mass. The kinetic freeze-out temperature is regarded as the intercept in the linear relation by us, which shows the same or similar tendency as those of effective temperature and chemical freeze-out temperature in the case of studying their dependences on centrality. The values in central collisions are larger than those in peripheral collisions, which renders that the interacting system in central collisions stays in a higher excitation state comparing with peripheral collisions at kinetic (or chemical) freeze-out.

c) The kinetic freeze-out temperature extracted by us in 0–20% Pb-Pb collisions at 2.76 TeV for including  $\pi^+$ ,  $K^+$ , and  $p$  is 0.091 GeV. Including  $d$  causes the kinetic freeze-out temperature increasing to 0.115 GeV, while including  $d$  and  $^3\text{He}$  causes the kinetic freeze-out temperature increasing to 0.148 GeV. The particle mass effects of kinetic freeze-out temperature for  $d$  and  $^3\text{He}$  are obvious. We think that we have observed an evidence of mass dependent differential kinetic freeze-out scenario or multiple kinetic freeze-out scenario.

d) We have also used an alternative method to extract the transverse flow velocity and flow velocity of the produced particles in the source rest frame based on the slopes in the linear relation between the mean transverse momentum and mean moving mass, as well as the mean momentum and mean moving mass. The particle mass effects of (transverse) flow velocity for  $d$  and  $^3\text{He}$  are not obvious, though light particles have larger (transverse) flow velocity. The transverse flow velocity and flow velocity obtained in the present work is close to  $0.5c$  and  $(\pi/2)0.5c$  respectively.

### Conflict of Interests

The authors declare that there is no conflict of interests regarding the publication of this paper.

### Acknowledgments

This work was supported by the National Natural Science Foundation of China under Grant No. 11575103 and the US DOE under contract DE-FG02-87ER40331.A008.

# References

- [1] J. Uphoff, O. Fochler, Z. Xu, C. Greiner, Acta Phys. Pol. B Proc. Supp. **5**, 555 (2012).
- [2] Y. Zhong, C.-B. Yang, X. Cai, S.-Q. Feng, Adv. High Energy Phys. **2015**, 193039 (2015).
- [3] S. Chatterjee, S. Das, L. Kumar, D. Mishra, B. Mohanty, R. Sahoo, N. Sharma, Adv. High Energy Phys. **2015**, 349013 (2015).
- [4] R. C. Hwa, Adv. High Energy Phys. **2015**, 526908 (2015).
- [5] G.-L. Ma, M.-W. Nie, Adv. High Energy Phys. **2015**, 967474 (2015).
- [6] D. D. Ivanenko, D. F. Kurdgelaidze, Astrofizika **1**, 479 (1965) [Astrophysics **1**, 251 (1965)].
- [7] N. Itoh, Prog. Theor. Phys. **44**, 291 (1970).
- [8] T. D. Lee, G. C. Wick, Phys. Rev. D **9**, 2291 (1974).
- [9] STAR Collaboration (L. Adamczyk *et al.*), Phys. Rev. C **92**, 024912 (2015).
- [10] R. A. Lacey, Phys. Rev. Lett. **114**, 142301 (2015).
- [11] M. Nasim, V. Bairathi, M. K. Sharma, B. Mohanty, A. Bhasin, Adv. High Energy Phys. **2015**, 197930 (2015).
- [12] R. J. Glauber, in *Lectures of Theoretical Physics*, edited by W. E. Brittin, L. G. Dunham, vol. 1, pp. 315–414 (Interscience, New York, NY, USA, 1959).
- [13] EMU01 Collaboration (M. I. Adamovich *et al.*), Eur. Phys. J. A **6**, 421 (1999).
- [14] P. B. Price, Y. D. He, Phys. Rev. C **43**, 835 (1991).
- [15] For the ALICE Collaboration (F. Barile), *Proceedings of the 3rd International Conference on New Frontiers in Physics*, (Kolymbari, Crete, Greece, July 28 – August 6, 2014), arXiv:1411.1941 [hep-ex] (2014).
- [16] ALICE Collaboration (J. Adam *et al.*), Phys. Rev. C **93**, 024917 (2016).
- [17] ALICE Collaboration (B. Abelev *et al.*) Phys. Rev. C **88**, 044910 (2013).
- [18] ALICE Collaboration (B. Abelev *et al.*), Phys. Rev. Lett. **109**, 252301 (2012).
- [19] Z. B. Tang, Y. C. Xu, L. J. Ruan, G. van Buren, F. Q. Wang, Z. B. Xu, Phys. Rev. C **79**, 051901(R) (2009).
- [20] S. Chatterjee, B. Mohanty, R. Singh, Phys. Rev. C **92**, 024917 (2015).
- [21] S. Chatterjee, B. Mohanty, Phys. Rev. C **90**, 034908 (2014).

- [22] D. Thakur, S. Tripathy, P. Garg, R. Sahoo, J. Cleymans, arXiv:1601.05223 [hep-ph] (2016).
- [23] C. Tsallis, J. Stat. Phys. **52**, 479 (1988).
- [24] T. S. Biró, G. Purcsel, K. Ürmösy, Eur. Phys. J. A **40**, 325 (2009).
- [25] J. Cleymans, D. Worku, Eur. Phys. J. A **48**, 160 (2012).
- [26] P. Z. Ning, L. Li, D. F. Min, *Foundation of Nuclear Physics: Nucleons and Nuclei*, (Higher Education Press, Beijing, China, 2003).
- [27] F.-H. Liu, Y.-Q. Gao, H.-R. Wei, Adv. High Energy Phys. **2014**, 293387 (2014).
- [28] F.-H. Liu, Y.-Q. Gao, T. Tian, B.-C. Li, Eur. Phys. J. A **50**, 94 (2014).
- [29] F.-H. Liu, J.-S. Li, Phys. Rev. C **78**, 044602 (2008).
- [30] F.-H. Liu, Nucl. Phys. A **810**, 159 (2008).
- [31] F. Büyükkiliç, D. Demirhan, Phys. Lett. A **181**, 24 (1993).
- [32] J.-C. Chen, Z.-P. Zhang, G.-Z. Su, L.-X. Chen, Y.-G. Shu, Phys. Lett. A **300**, 65 (2002).
- [33] J. M. Conroy, H. G. Miller, Phys. Rev. D **78**, 054010 (2008).
- [34] F. Pennini, A. Plastino, A. R. Plastino, Phys. Lett. A **208**, 309 (1995).
- [35] A. M. Teweldeberhan, A. R. Plastino, H. G. Miller, Phys. Lett. A **343**, 71 (2005).
- [36] J. M. Conroy, H. G. Miller, A. R. Plastino, Phys. Lett. A **374**, 4581 (2010).
- [37] H. Zheng, L.-L. Zhu, Adv. High Energy Phys. **2016**, 9632126 (2016).
- [38] H. Zheng, L.-L. Zhu, Adv. High Energy Phys. **2015**, 180491 (2015).
- [39] A. Andronic, P. Braun-Munzinger, J. Stachel, Nucl. Phys. A **834**, 237c (2010).
- [40] U. W. Heinz, *Lecture Notes for Lectures Presented at the 2nd CERN – Latin-American School of High-Energy Physics*, (San Miguel Regla, Mexico, June 1-14, 2003), arXiv:hep-ph/0407360 (2004).
- [41] PHENIX Collaboration (S. S. Adler *et al.*), Phys. Rev. C **69**, 034909 (2004).
- [42] S. Takeuchi, K. Murase, T. Hirano, P. Huovinen, Y. Nara, Phys. Rev. C **92**, 044907 (2015).
- [43] R. Russo, Ph.D. thesis, (Universitaâ degli Studi di Torino, Italy, 2015), arXiv:1511.04380 [nucl-ex] (2015).
- [44] E. Schnedermann, J. Sollfrank, U. W. Heinz, Phys. Rev. C **48**, 2462 (1993).

- [45] STAR Collaboration (J. Adams *et al.*), Nucl. Phys. A **757**, 102 (2005).
- [46] ALICE Collaboration (B. Abelev *et al.*), Phys. Rev. C **88**, 044910 (2013).
- [47] H.-R. Wei, F.-H. Liu, R. A. Lacey, Eur. Phys. J. A **52**, 102 (2016).